

Vortex deformation and breaking in superconductors: A microscopic description

E. Pardo^{a,b}, J. H. Durrell^a and M. G. Blamire^a

^aDepartment of Materials Science and Metallurgy,
University of Cambridge, Pembroke Street, Cambridge,
CB2 3QZ, United Kingdom

^bGrup d'Electromagnetisme, Departament de Física,
Universitat Autònoma de Barcelona, 08193 Bellaterra,
Barcelona, Catalonia, Spain

September 30, 2018

Abstract

Vortex breaking has been traditionally studied for nonuniform critical current densities, although it may also appear due to nonuniform pinning force distributions. In this article we study the case of a high-pinning/low-pinning/high-pinning layered structure. We have developed an elastic model for describing the deformation of a vortex in these systems in the presence of a uniform transport current density J for any arbitrary orientation of the transport current and the magnetic field. If J is above a certain critical value, J_c , the vortex breaks and a finite effective resistance appears. Our model can be applied to some experimental configurations where vortex breaking naturally exists. This is the case for $\text{YBa}_2\text{Cu}_3\text{O}_{7-\delta}$ (YBCO) low angle grain boundaries and films on vicinal substrates, where the breaking is experienced by Abrikosov-Josephson vortices (AJV) and Josephson string vortices (SV), respectively. With our model, we have experimentally extracted some intrinsic parameters of the AJV and SV, such as the line tension ϵ_l and compared it to existing predictions based on the vortex structure.

Contents

1	Introduction	2
2	General considerations	3
2.1	Elastic model	3
2.2	On the line tension	4
3	Analytical limits	5
3.1	Applied field perpendicular to the current flow	5
3.1.1	Infinite pinning force in the high pinning region	5
3.1.2	Finite pinning force in the high pinning region	8
3.2	Applied field parallel to the current flow	9
4	Numerical approach	11
4.1	Vortex line calculation	12
4.2	Critical current calculation	12
4.3	Results	13
4.3.1	Vortex bending	13
4.3.2	Critical current density	13

5	Application to experimental situations	16
5.1	Low-angle grain boundaries	16
5.1.1	Comparison with experiments	17
5.2	YBCO films with miscut substrate	18
5.2.1	Breaking description for vicinal films	18
5.2.2	Comparison with experiments	19
6	Conclusions	20

1 Introduction

The study of vortex physics has been an important topic in superconductivity research since the prediction of the existence of superconducting vortices by Abrikosov [1, 2, 3, 4]. Superconducting vortices have been the subject of many theoretical studies including those addressing the vortex line energy [5, 6], single vortex interactions [7, 8, 9, 10] and vortex lattice interactions [11, 12, 13, 14].

One way to measure the properties of a vortex, such as the vortex line tension ϵ_l is by means of vortex breaking experiments. These kind of experiments were initially performed by using a nonuniform transport current in order to create a nonuniform driving force in the vortex length thus bending the vortex and, for large enough current density difference, break (or cut) the vortex [15, 16, 17, 19, 18]. Another way in which vortex breaking may be observed is where vortices are subject to an inhomogenous pinning force in the presence of a uniform transport current. In this article, we study the microscopic bending and breaking process for the situation where the vortex crosses a low-pinning region (LPR) of thickness d compressed by two high-pinning ones (HPR) with a uniform transport current \mathbf{J} and a magnetic field \mathbf{B} with an arbitrary orientation, Fig. 1. In order to perform this study, an elastic model is developed assuming isotropic vortices with a constant line tension ϵ_l towards deformations. Using this model, we propose a vortex breaking process in the depressed pinning region. Afterwards, a $J_c(\theta, \varphi)$ dependence is obtained, where θ and φ are the angles defining the orientation of the applied field (see Fig. 1), as a function of the elastic force per unit length and the pinning line forces in either the LPR and the HPR.

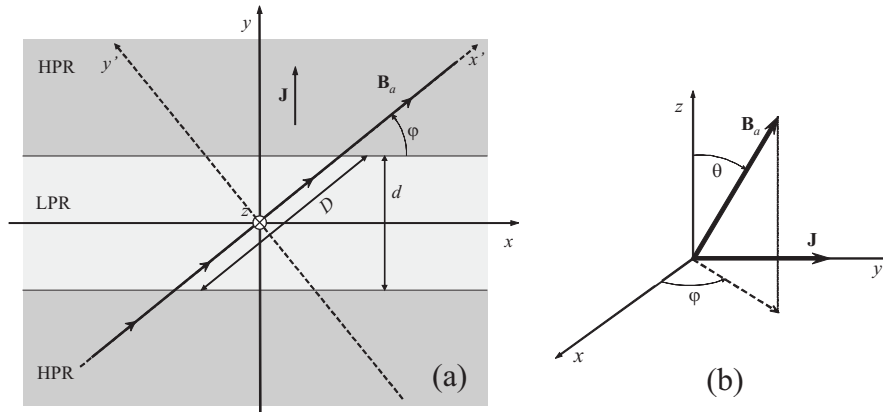


Figure 1: (a) Sketch of an undeformed vortex line in a depressed pinning layer, consisting of a low pinning region (LPR) bounded by high pinning ones (HPR). The applied field \mathbf{B}_a makes an angle with both the LPR-HPR interface and \mathbf{J} . The vortex length in the LPR, D , is $D = d/|\sin \theta \sin \varphi|$. (b) Definition of the angular coordinates φ and θ .

The geometry described in this article can be directly applied in order to model experimental situations like low-angle grain boundaries (LAGB) in $\text{YBa}_2\text{Cu}_3\text{O}_{7-\delta}$ (YBCO) bicrystals or YBCO films on a miscut substrate (commonly named vicinal films), as discussed in Sec. 5. It is worth noting that, according to Gurevich *et al* [20] the vortices in high-temperature superconductor LAGB for crystal misorientation angles up to 23° are not conventional Abrikosov vortices (AV) but Abrikosov-Josephson vortices (AJV)¹. Moreover, the vortices that it is possible to break in YBCO vicinal films are string vortices (SV) lying between the ab planes, which are of Josephson nature. In this paper, the vortex line tension ϵ_l in these systems is found by fitting the theoretically obtained $J_c(\theta, \varphi)$ dependence to measured data. Then, thanks to the model developed in this work, it is possible to extract the line tension of exotic superconductors of Josephson and Abrikosov-Josephson nature, which physical properties are still not very well known.

The article is structured as follows. First, some general features of our problem, including the basis of the elastic model, are discussed in Sec. 2. In Sec. 3 we deduce the analytical limits of the vortex deformation and critical current density for the studied HPR/LPR/HPR structure at two specific magnetic field orientations: \mathbf{B} perpendicular or parallel to \mathbf{J} , with \mathbf{J} crossing the HPR/LPR boundary. In the following section, Sec. 4, we introduce a numerical procedure for solving the problem for any field and current orientation and we present general normalized results. Next, Sec. 5, the model is applied to the experimental situations of LAGB in YBCO bicrystals and vicinal films in order to obtain the AJV and SV vortex line tension, respectively. In that section, it is also discussed the flux breaking process in a vicinal film. Finally, we present our conclusions in Sec. 6.

2 General considerations

In this section we discuss some general features of our system, such as the basis of the elastic model and the properties of the vortex line energy.

2.1 Elastic model

We simulate the behaviour of a vortex line as an string with constant line energy ϵ_l . Thus, its total energy is

$$E = \epsilon_l \int_C dl = \epsilon_l \int_C d\tau |\partial_\tau \mathbf{r}|, \quad (1)$$

where C is the vortex line path, l is the line length and τ is a parametrization of C . If the vortex follows a straight line, the elastic force at the vortex ends is

$$\mathbf{F}_e = \pm \mathbf{e}_l dE/dl = \pm \epsilon_l \mathbf{e}_l, \quad (2)$$

where \mathbf{e}_l is the unit vector locally parallel to the vortex line:

$$\mathbf{e}_l(\tau) = \frac{\partial_\tau \mathbf{r}}{|\partial_\tau \mathbf{r}|}. \quad (3)$$

From Eq. (2) it is clear that for an isotropic string the line tension equals to the line energy. The local elastic force per unit length $\mathbf{f}_e(\tau)$ for a deformed vortex can be deduced by approximating the vortex line into a set of straight segments and using that the net elastic force at a junction between segments is

$$\delta \mathbf{F}_e(\tau) = \epsilon_l [\mathbf{e}_l(\tau) - \mathbf{e}_l(\tau - \delta\tau)], \quad (4)$$

¹Actually, the structure of a vortex in a LAGB for anisotropic superconductors is more complex than the AJV described in [20]. The vortex nature in our studied situation is discussed in Sec. 5.1.

where $\delta\tau$ is a variation in τ and $\delta\mathbf{F}_e(\tau)$ is the elastic force in the junction between the vortex segments corresponding to τ and $\tau - \delta\tau$. After making the limit of $\delta\tau \rightarrow 0$, the force per unit length can be found as

$$\mathbf{f}_e(\tau) = \frac{\epsilon_l}{|\partial_\tau \mathbf{r}|^4} \partial_\tau \mathbf{r} \times (\partial_\tau^2 \mathbf{r} \times \partial_\tau \mathbf{r}). \quad (5)$$

Apart from the elastic force, the vortex is submitted to a driving force, \mathbf{F}_d , due to a macroscopic current density \mathbf{J} . The line force density of this force, \mathbf{f}_d , is

$$\mathbf{f}_d = \Phi_0 \mathbf{J} \times \mathbf{e}_l, \quad (6)$$

where Φ_0 is the flux quantum, that in SI is $\Phi_0 = \pi \hbar e$.

For superconductors with pinning we should also take into account the pinning force per unit length \mathbf{f}_p , which has a certain maximum magnitude $f_{p,m}$. This force opposes any local movement of the vortex line, so that it will follow the direction of the elastic and the driving forces. This description of the pinning behaviour implicitly assumes that \mathbf{f}_p is due to many weak pinning centres uniformly distributed in the vortex length, rather than few strong pinning sites. The latter scenario would result in a more complicated bending behaviour.

The equilibrium vortex configuration will be that one which results in a null net force per unit length at any point. Thus, from Eqs. (5) and (6) we find the differential equation of the vortex line

$$\frac{\epsilon_l}{|\partial_\tau \mathbf{r}|^4} \partial_\tau \mathbf{r} \times (\partial_\tau^2 \mathbf{r} \times \partial_\tau \mathbf{r}) + \Phi_0 \mathbf{J} \times \mathbf{e}_l + \mathbf{f}_p = 0. \quad (7)$$

2.2 On the line tension

We next discuss the dependence of the line tension ϵ_l on the superconductor internal parameters for both an isotropic and anisotropic Abrikosov vortex (AV).

For an isolated isotropic AV, the line tension corresponds to the energy per unit length, which has been investigated by several authors [5, 3, 6]. Following the numerical calculations of Hu [6], ϵ_l in the approximation of high Ginzburg-Landau parameter κ is

$$\epsilon_l = \epsilon_{l,0} (\ln \kappa + 0.4968), \quad (8)$$

where $\epsilon_{l,0} = (\Phi_0/\lambda)^2/(4\pi\mu_0)$ and λ is the magnetic penetration depth. A more general, although maybe less accurate, analytical expression for arbitrary κ was obtained by Clem [5] using a variational approach. That expression, however, is still proportional to $\epsilon_{l,0}$.

A vortex in a flux line lattice has a different line tension. In general, ϵ_l depends on the vortex separation, a_0 , and the characteristic deformation wavelength, l_d [3, 4]. The qualitative behaviour is that ϵ_l decreases with decreasing both a_0 and l_d . However, for magnetic fields such that $a_0 \ll \lambda$ and $a_0 \gg \xi$, the line tension is roughly constant (where ξ is the superconductor coherence length). In a simplified way, this can be explained as follows: if $a_0 \ll \lambda$ the magnetic field and the supercurrent density is roughly uniform between the vortices except close to the vortex core. Then, the energy variation per unit length due to a deformation is just the core energy per unit length and, consequently, it does not depend on the magnetic field. Following [10], ϵ_l for the London limit is $\epsilon_l = \epsilon_{l,0} \int_1^\infty dx (e^{-x/\kappa})/\sqrt{x^2 - 1} + \epsilon_{l,c} = \epsilon_{l,0} K_0(1/\kappa) + \epsilon_{l,c}$, where $\epsilon_{l,c}$ is the core energy per unit length and K_0 is the modified Bessel function of order 0. Comparing with Eq. (8), we obtain that

$$\epsilon_{l,c} = \epsilon_{l,0} [\ln \kappa + 0.4968 - K_0(1/\kappa)]. \quad (9)$$

For the limit of $\kappa \gg 1$, Eq. (9) becomes² $\epsilon_{l,c} = 0.3809\epsilon_{l,0}$, so that we obtain a line tension of the order of $\epsilon_{l,0}$.

²The approximation of $\kappa \gg 1$ produces an error smaller than a 1% for $\kappa \geq 20$.

In Sec. 5 we study the line tension in SVs in YBCO, for which ϵ_l is essentially the same as an anisotropic Abrikosov vortex [3, 4]. Following Ref. [3], the line tension for an anisotropic vortex parallel to the ab planes with $\kappa \gg 1$ and $^3 l_d \ll \lambda_{ab}$, where λ_{ab} is the penetration depth for the ab planes, is approximately

$$\epsilon_l^\perp \approx \Gamma \frac{\Phi_0^2}{4\pi\mu_0\lambda_{ab}^2} \quad (10)$$

$$\epsilon_l^\parallel \approx \frac{1}{\Gamma} \frac{\Phi_0^2}{4\pi\mu_0\lambda_{ab}^2}, \quad (11)$$

where ϵ_l^\perp and ϵ_l^\parallel are for deformations in the c and ab directions, respectively, and Γ is the material anisotropy factor $\Gamma = \lambda_c/\lambda_{ab} > 1$ (for YBCO, $\Gamma \approx 5$), where λ_c is the penetration depth in the c axis.

3 Analytical limits

In this section we analytically describe the limits of $\varphi \rightarrow 0$ with $\theta = \pi/2$ (\mathbf{B} perpendicular to \mathbf{J}) and $\varphi \rightarrow \pi/2$ with $\theta = \pi/2$ (\mathbf{B} parallel to \mathbf{J}).

3.1 Applied field perpendicular to the current flow

In the following, we suppose that \mathbf{B} is almost parallel to the HPR-LPR interface, that is very low φ and $\theta = \pi/2$, Fig. 1. For this case, the applied field is approximately perpendicular to the current flow, so that the vortex bows in the z direction only. This is consistent with the numerical calculations in Sec. 4.3 below.

Let define the axis x' as that in the direction of the applied field and y' as that in the direction of $\mathbf{e}_z \times \mathbf{e}_{x'}$, Fig. 1. Taking the coordinate x' as the vortex line parameter, its positions are

$$\mathbf{r}(x') = x'\mathbf{e}_{x'} + z(x')\mathbf{e}_z, \quad (12)$$

so that the $z(x')$ dependence uniquely describes the vortex line. Using this parametrization, it can be seen from Eq. (5) that the elastic force per unit length is in the $\mathbf{e}_{y'} \times \mathbf{e}_l$ direction and, thus, it can only compensate the driving force in this direction. Therefore, the relevant component of the driving force is $\Phi_0[\mathbf{J} \cdot \mathbf{e}_{y'}]\mathbf{e}_{y'} \times \mathbf{e}_l = \Phi_0 J \cos \varphi \mathbf{e}_{y'} \times \mathbf{e}_l$. The differential equation for the vortex line of Eq. (7) becomes

$$J\Phi_0 \cos \varphi - \epsilon_l \left[1 + \left(\frac{dz}{dx'} \right)^2 \right]^{-3/2} \frac{d^2z}{dx'^2} + f_p = 0. \quad (13)$$

3.1.1 Infinite pinning force in the high pinning region

In order to simplify the system, we assume that the maximum pinning force per unit length in the high pinning region is much higher than any other line forces in the problem, i. e. the pinning force in the low pinning region, the driving force and the elastic force. With this approximation, the vortex in the HPR follows a straight line in the \mathbf{B} direction for any \mathbf{J} . Thus, we only have to obtain the vortex line configuration in the LPR. First, we study the case of null pinning force in the LPR and afterwards we include the effect of a finite $f_{p,m}$.

³For our experimentally studied situations of Sec. 5, the condition $l_d \ll \lambda_{ab}$ is satisfied for $\varphi > 5^\circ$ and $\theta > 0.5^\circ$ for LAGB and vicinal films, respectively.

Assuming null pinning force, the differential equation (13) can be solved by direct integration. For doing this, Eq. (13) must be first solved for $\frac{dz}{dx'}(x')$ and then for $z(x')$ with a result

$$z(x') = k_1 - \sqrt{R^2 - (x' + k_2)^2}, \quad (14)$$

where R is defined as $R = \epsilon_l / (|\cos \varphi| J \Phi_0)$ and k_1 and k_2 are integration constants. These constants can be found taking into account that the vortex line in the HPR is fixed, obtaining that

$$z(x') = \sqrt{R^2 - (D/2)^2} - \sqrt{R^2 - x'^2}, \quad (15)$$

where $D = d / |\sin \theta \sin \varphi|$ is the length of a straight vortex in the LPR (Fig. 1). From Eq. (15) we see that the vortex line bents forming a circular arch with radius R . The elastic and driving forces per unit length are calculated from Eqs. (5), (6) and (15), yielding the result

$$\mathbf{f}_e = -\frac{\epsilon_l}{R} \mathbf{e}_{y'} \times \mathbf{e}_l \quad (16)$$

$$\mathbf{f}_d = \cos \varphi \Phi_0 J \mathbf{e}_{y'} \times \mathbf{e}_l. \quad (17)$$

From these equations we see that \mathbf{f}_e and \mathbf{f}_d have uniform magnitude and are perpendicular to the vortex line. The elastic force per unit length is inversely proportional to the curvature radius R . Therefore, the maximum $|\mathbf{f}_e|$ that the vortex is able to produce, $f_{e,m}$, is

$$f_{e,m} = 2\epsilon_l / D \quad (18)$$

that leads to a critical J , J_c , as

$$J_c = \frac{2\epsilon_l}{\Phi_0 D \cos \varphi} = \frac{2\epsilon_l}{\Phi_0 d} \tan |\varphi|, \quad (19)$$

Where at the second equality we used that $D = d / \sin |\varphi|$ for $\theta = \pi/2$ (Fig. 1). For J lower than J_c the vortex line is stable, while for $J > J_c$ it cannot balance the driving force and the vortex line breaks, Fig. 2. For $J > J_c$, Fig. 2(c), there is a straight horizontal vortex segment in the border between the HPR and LPR because in this place the driving force pushes the vortex towards the HPR, where the available pinning force is very large and, thus, fully compensates the driving force.

The breaking process is completed if the horizontal vortex segment cross-joins and recombines [7, 9, 10] with the fixed part of the neighbouring vortex. This will happen when the driving force overcomes the repulsion between these two segments. Indeed, not only is the repulsion between vortices at right angles strongly suppressed but also the interaction force becomes attractive for separations close to ξ for any orientation [7, 9]. The expected situation after cross-joining is that the vortex segment in the LPR joins with the undeformed neighbouring one and there appear two horizontal antiparallel vortex lines. These horizontal vortices will experience a strong attraction which can overcome the pinning and driving forces, so that the vortices move towards each other and annihilate. In the case that the vortex attraction is not strong enough, the elongation and recombination process repeats, creating horizontal vortices with multiple vorticity. These vortices have a larger core and, thus, present a lower pinning line force and their mutual attraction is larger. At some moment these horizontal vortices will detach from the HPR-LPR border and annihilate to each other. Afterwards, the breaking and cross-joining process is repeated.

For large enough magnetic fields, i. e. low vortex separations, there can be vortex cross-joining for J below that of maximum vortex deformation when the distance between the vortex arc in the LPR and the straight part of the next vortex is of the order of ξ .

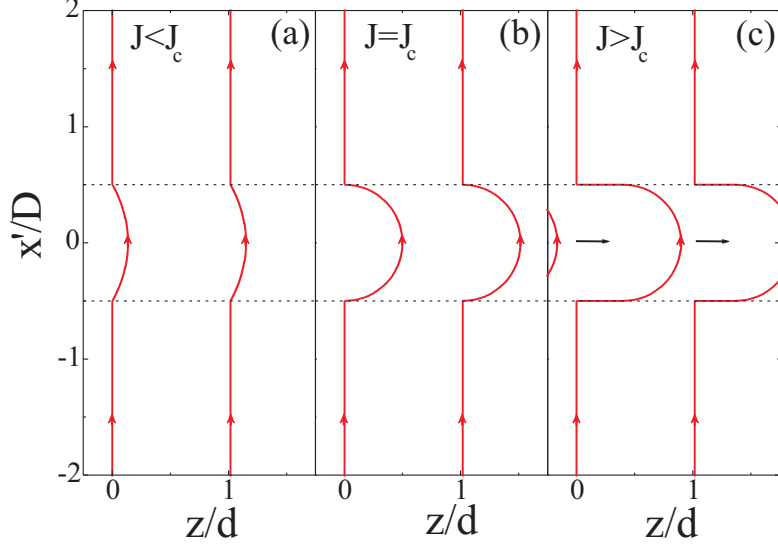


Figure 2: Vortex bowing for the situation of Fig. 1 with $\theta = \pi/2$, $\varphi \ll \pi/2$ and infinite maximum pinning force per unit length in the HPR. The graphs correspond to $J < J_c$ (a), $J = J_c$ (b) and $J > J_c$ (c) from left to right.

Let define the vortex breaking force F_{break} as the required driving force magnitude necessary to break the vortex in absence of pinning in the LPR. Using Eqs. (3) and (6) we find that the driving force is

$$\begin{aligned} \mathbf{F}_d &= \int_{\text{LPR}} d\mathbf{l} \mathbf{f}_d = \int_{-D/2}^{D/2} dx' |\partial_{x'} \mathbf{r}| \cos \varphi \Phi_0 J \mathbf{e}_y \times \frac{\partial_{x'} \mathbf{r}}{|\partial_{x'} \mathbf{r}|} \\ &= \cos \varphi \Phi_0 J \mathbf{e}_y \times \int_{-D/2}^{D/2} dx' \partial_{x'} \mathbf{r} = -\cos \varphi \Phi_0 J D \mathbf{e}_z. \end{aligned} \quad (20)$$

The breaking force is obtained by taking $J = J_c$ and using Eqs. (19) and (20), with a result

$$F_{\text{break}} = 2\epsilon_l. \quad (21)$$

We next consider the presence of a pinning force in the LPR as follows. If the driving force per unit length is lower than $f_{p,m}$, the pinning force per unit length counteracts the driving force and the vortex stays as a straight line. Otherwise, the vortex bows and the elastic force per unit length compensates the remaining force. For this situation, the vortex line follows Eq. (13) with $f_p = -f_{p,m}$. Taking this into account, the vortex configuration still follows Eqs. (14) and (15) but with a curvature radius $R = \epsilon_l / (|\cos \varphi| J \Phi_0 - f_{p,m})$. Thus, Eqs. (16)-(18) are still valid but now J_c is

$$J_c = \frac{2\epsilon_l}{\Phi_0 d} \tan |\varphi| + \frac{f_{p,m}}{\Phi_0 |\cos \varphi|}. \quad (22)$$

This equation is equivalent to that deduced by Durrell *et al* in [21, 22], if it is taken into account that $F_{\text{break}} = 2\epsilon_l$.

The vortex line of Fig. 2 is nonderivable at the border of the LPR and HPR. Then, on these points there acts a net elastic force with magnitude $|\mathbf{F}_e| = \epsilon_l |\mathbf{e}_{x'} - \mathbf{e}_l(x' = d/2)|$ [Eq. (4)] which can only be balanced by a finite pinning force. Such a pinning force is possible under the assumption of infinite maximum pinning force per unit length in the HPR, $f_{p,m}^*$. If $f_{p,m}^*$ is limited to a finite value, the vortex line must be derivative at every point. Thus,

the vortex can bow in the HPR even if the driving force per unit length is lower than $f_{p,m}^*$. However, the main features of the vortex breaking remain the same.

We contemplate a finite pinning force per unit length in the HPR in the following section.

3.1.2 Finite pinning force in the high pinning region

We next relax the assumption of infinite maximum pinning force per unit length in the HPR, $f_{p,m}^*$.

The vortex configuration $z(x')$ still follows the differential equation (13) but now f_p depends on the position. For $f_{p,m}^* > \Phi_0 J > f_{p,m}$, the vortex line in the LPR bows in the direction of the driving force and, then, $f_p = -f_{p,m}$ there. The pinning force per unit length in the HPR can, in principle, take any value between $-f_{p,m}^*$ and $f_{p,m}^*$. If the transport current density is reached by increasing its value from 0 to J in a quasistatic speed, the vortex line progressively deforms from a straight line to its final stable configuration. In this process the pinning force density opposes with its maximum value to the driving force. Thus, in the HPR $f_p = f_{p,m}^*$.

Taking this into account, we solve Eq. (13) using that the vortex line must be continuous and smooth at the LPR and HPR boundaries, with the result

$$z(x') = \begin{cases} 0 & \text{for } x' < -x'_0 \\ \sqrt{R^{*2} - (x' + x'_0)^2} - R^* & \text{for } -x'_0 < x' < -D/2 \\ -\sqrt{R^2 - x'^2} + (2x'_0/D)\sqrt{R^2 - D^2/4} - R^* & \text{for } -D/2 < x' < D/2 \\ \sqrt{R^{*2} - (x' - x'_0)^2} - R^* & \text{for } D/2 < x' < x'_0 \\ 0 & \text{for } x'_0 < x' \end{cases} \quad (23)$$

with

$$R = \epsilon_l / (|\cos \varphi| J \Phi_0 - f_{p,m}) \quad (24)$$

$$R^* = \epsilon_l / (f_{p,m}^* - |\cos \varphi| J \Phi_0) \quad (25)$$

$$x'_0 = (D/2)(1 + R^*/R). \quad (26)$$

The quantity x'_0 is the minimum $|x'|$ for which the vortex is not deformed and R and R^* are the curvature radii in the LPR and the HPR, respectively.

The vortex breaking process for this situation is shown in Figs. 3 and 4, where we took $f_{p,m}^*/f_{p,m} = 9$ and $2\epsilon_l/(df_{p,m}) = 18.6$, corresponding to the experimental situation in Fig. 8. From Figs. 3 and 4 we can see that the breaking process is essentially the same as for infinite $f_{p,m}^*$ (Fig. 2). However, for J below that of maximum elastic force, the vortex bending could cause a local separation between neighboring vortices smaller than ξ . This would reduce J_c compared with the predicted one from elasticity considerations. For our experimental situation in Sec. 5.1, the minimum vortex distance at $J = J_c$ is around 2ξ so that the expected cross-joining is still at the breaking critical current density.

For local vortex separations larger than ξ , such as those in Figs. 3 and 4 the limiting J_c mechanism is basically the same as for infinite $f_{p,m}^*$ (Fig. 2). Thus, Eq. (18) for the maximum elastic line force is still valid. However, in order to observe breaking for finite $f_{p,m}^*$, it is not enough that f_d overcomes $f_{p,m}$ but also

$$f_{p,m}^* > f_{p,m} + f_{e,m} = f_{p,m} + 2\epsilon_l |\sin \varphi| / d. \quad (27)$$

This can be seen as follows. The driving force per unit length is uniform in the vortex which, from the equilibrium condition in the LPR it is $f_d = f_{p,m} + f_{e,m}$. Then, if $f_{p,m}^* < f_d = f_{p,m} + f_{e,m}$, there is depinning in the HPR and there is no vortex breaking. Moreover, from equation (27) it can be seen that $2\epsilon_l/d > f_{p,m}^* - f_{p,m}$ there will be breaking or depinning in

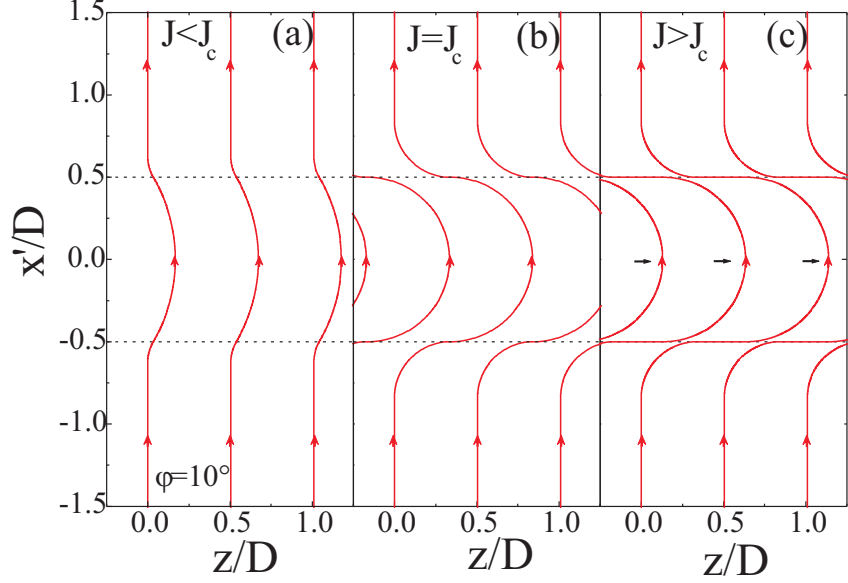


Figure 3: Vortex bowing for the situation of Fig. 1 with $\theta = \pi/2$, $\varphi = 10^\circ$ and a finite maximum pinning force in both the LPR and HPR $f_{p,m}$ and $f_{p,m}^*$, respectively. The graphs are for $f_{p,m}^*/f_{p,m} = 9$, $2\epsilon_l/(df_{p,m}) = 18.6$, $d = 10\text{nm}$ and $B = 6\text{T}$, corresponding to the experimental situation in Fig. 8. Half the number of vortices have been plot for a better visualization.

the HPR, depending on the value of φ . Thus, from Eqs. (22) and (27), the $J_c(\varphi)$ dependence will be

$$J_c(\varphi) = \begin{cases} J_c = \frac{2\epsilon_l}{\Phi_0 d} \tan |\varphi| + \frac{f_{p,m}}{\Phi_0 |\cos \varphi|} & \text{for } \varphi < \varphi_d \\ J_c = \frac{f_{p,m}^*}{\Phi_0 |\cos \varphi|} & \text{for } \varphi \geq \varphi_d \end{cases} \quad (28)$$

with

$$\varphi_d = \arcsin \frac{f_{p,m}^* - f_{p,m}}{2\epsilon_l/d}. \quad (29)$$

Another difference with the assumption of infinite $f_{p,m}^*$ is that now the vortex significantly bends in the HPR, with a maximum deformation at $J = J_c$. The curvature radius in the HPR at $J = J_c$, R_c^* , can be deduced from Eqs. (25) and (22), with a result

$$R_c^*/d = \frac{\epsilon_l}{f_{p,m}^* - f_{p,m} - \frac{2\epsilon_l}{d} |\sin \varphi|}. \quad (30)$$

The value of R_c^*/d is finite for the limit $\varphi = 0$ and R_c^*/d approaches to infinite when $|\varphi| = \varphi_d$. The behaviour of R_c^*/d as a function of φ is plotted in Fig. 5 for $2\epsilon_l/(df_{p,m}) = 19$ and $f_{p,m}^*/f_{p,m} = 5, 10, 15, 20, 25$ and 30 in the arrow direction. The angle φ_d , calculated from Eq. (29), is $12.2, 28.3, 47.5$ and 90° for $f_{p,m}^*/f_{p,m} = 5, 10, 15$ and 20 , respectively. In Fig. 5 it can be seen that R_c^* diverges when it approaches to φ_d but it has no discontinuities for $2\epsilon_l/(df_{p,m}) < f_{p,m}^*/f_{p,m} - 1$.

3.2 Applied field parallel to the current flow

We next describe the situation that the applied field is parallel to the current flow, usually known as the force-free configuration. For simplicity, we only study the case of infinite pinning force per unit length in the HPR and no pinning in the LPR.

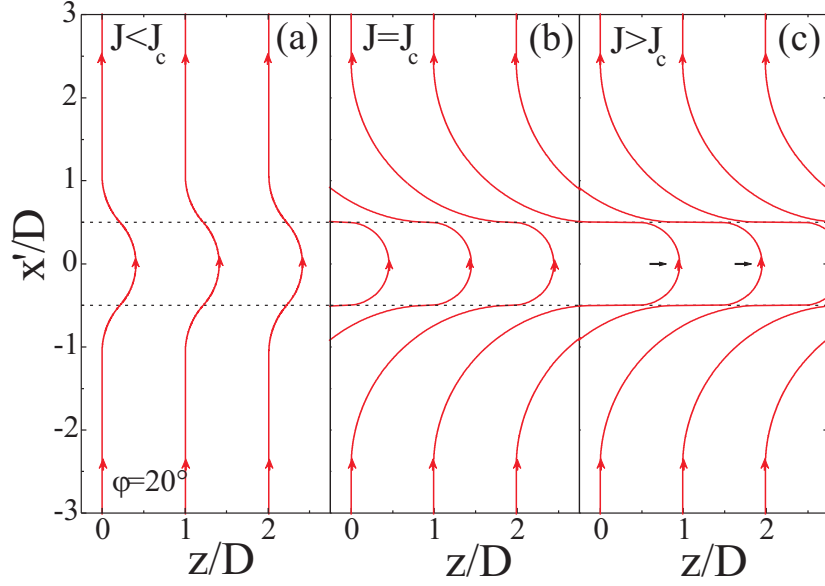


Figure 4: The same as Fig. 3 but for $\varphi = 20^\circ$.

This geometry corresponds to $\varphi = \theta = \pi/2$ in Fig. 1, so that $\mathbf{B} = B\mathbf{e}_y$. Taking y as the vortex line parameter, the differential equation (7) turns into

$$\frac{(\partial_y^2 x \mathbf{e}_x + \partial_y^2 z \mathbf{e}_z)}{\sqrt{1 + (\partial_y x)^2 + (\partial_y z)^2}} + \frac{\Phi_0 J}{\epsilon_l} (\partial_y z \mathbf{e}_x - \partial_y x \mathbf{e}_z) = 0. \quad (31)$$

For the force-free configuration, it has been found that the vortices are susceptible to become spirals [23, 24]. Moreover, our numerical results below (Fig. 6 in Sec. 4) show that for a \mathbf{B} almost parallel to \mathbf{J} , the vortex line configuration is an spiral with twist pitch $-d$. The spiral must cross the y axis at $y = \pm d/2$ for continuity with the vortex line in the HPR. A spiral following these features is

$$\mathbf{r}(y) = a \left(1 + \cos \frac{2\pi y}{d} \right) \mathbf{e}_x + y \mathbf{e}_y + a \sin \frac{2\pi y}{d} \mathbf{e}_z, \quad (32)$$

where a is the radius of the spiral. This spiral follows Eq. (31) and, thus, it describes a static vortex configuration. The spiral of Eq. (32) has the axis in the y direction but displaced a vector $a\mathbf{e}_x$ from it. Actually, any rotation of the spiral from Eq. (32) around the y direction is also a static vortex configuration. The elastic and driving forces per unit length for these spiral vortex lines are

$$\mathbf{f}_e = -\epsilon_l \frac{\frac{4a\pi^2}{d^2}}{1 + \left(\frac{2a\pi}{d}\right)^2} \mathbf{e}_t \quad (33)$$

$$\mathbf{f}_d = J\Phi_0 \frac{\frac{2a\pi}{d}}{\sqrt{1 + \left(\frac{2a\pi}{d}\right)^2}} \mathbf{e}_t \quad (34)$$

with

$$\mathbf{e}_t = \cos \left(\frac{2\pi y}{d} - \phi \right) \mathbf{e}_x + \sin \left(\frac{2\pi y}{d} - \phi \right) \mathbf{e}_z. \quad (35)$$

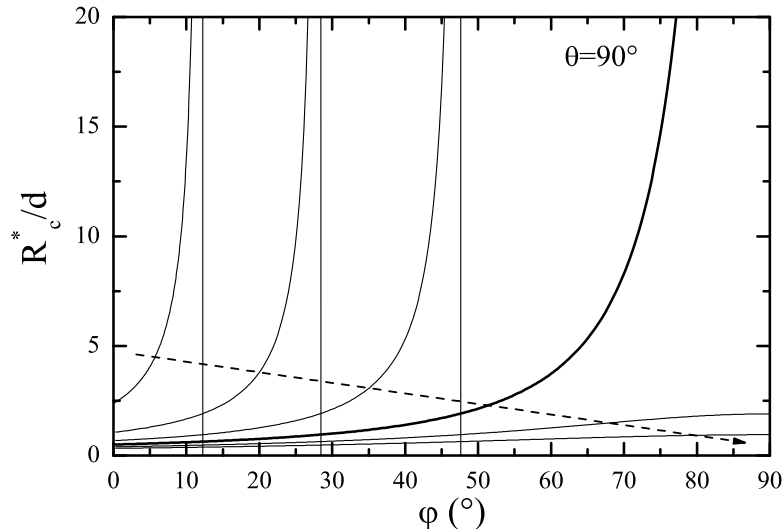


Figure 5: Vortex line radius in the HPR for $J = J_c$ normalized to d , R_c^*/d , as a function of φ (Fig. 1) for $2\epsilon_l/(df_{p,m}) = 19$ and $f_{p,m}^*/f_{p,m} = 5, 10, 15, 20, 25, 30$ in the arrow direction. The line for $f_{p,m}^*/f_{p,m} = 20$ diverges for $\varphi = 90^\circ$.

The radius at which there is equilibrium a_{eq} is deduced from Eqs. (33) and (34) and considering $\mathbf{f}_e + \mathbf{f}_d = 0$, obtaining

$$a_{\text{eq}} = \sqrt{\left(\frac{\epsilon_l}{J\Phi_0}\right)^2 - \left(\frac{d}{2\pi}\right)^2}. \quad (36)$$

By examination of Eqs. (33) and (34) we see that the vortex at $a = a_{\text{eq}}$ is in unstable equilibrium. Indeed, a radius slightly smaller than a_{eq} presents an elastic force higher than the driving force and the spiral shrinks until it becomes an straight line. For $a > a_{\text{eq}}$ the driving force is higher than the elastic one and the vortex expands indefinitely. However, any equilibrium is not possible when J is high enough to produce an a_{eq} from Eq. (36) with null or imaginary values. The minimum J value at which this occurs, J_c , is

$$J_c = \frac{2\pi\epsilon_l}{d\Phi_0}. \quad (37)$$

Comparing J_c for the parallel and the perpendicular cases, Eqs. (19) and (37), we see that for the same vortex length in the LPR J_c for the force-free situation is only π times higher than that one for a perpendicular field.

4 Numerical approach

In this section a numerical model is introduced in order to calculate the vortex deformation in a depressed pinning layer, Fig. 1, at any orientation of the macroscopic current density \mathbf{J} and the applied magnetic field \mathbf{B} . As for the analytical approximation, we consider an elastic model for the vortex line. In order to simplify the analysis, we assume the approximation of infinite maximum pinning force per unit length in the HPR, $f_{p,m}^* \rightarrow \infty$, for the numerical calculations. As shown above, Sec. 3.1.2, taking into account a finite $f_{p,m}^*$ does not substantially change the J_c results.

4.1 Vortex line calculation

We next outline the numerical method used for calculating the vortex line configuration. In order to generalize the procedure for several applications, we consider a vortex segment of length d strongly pinned at its ends, beyond them the vortex line is straight and follows the applied field direction.

The vortex configuration is calculated by physical evolution in a similar way as in [10], as follows.

We take the initial state of a straight vortex in the applied field direction and we divide the pinning-free segment into n identical line elements. In the following discussion we term the boundary between elements as a *node*. Then, we calculate the forces per unit length \mathbf{f}_e , \mathbf{f}_d and \mathbf{f}_p corresponding to each node and change the node position proportionally to the resulting line force. That is, the position of the node labelled as i at the time instant k , $\mathbf{r}_{i,k}$, is calculated from the previous time instant as

$$\mathbf{r}_{i,k} = \mathbf{r}_{i,k-1} + \Delta_k[\mathbf{f}_e(\mathbf{r}_{i,k-1}) + \mathbf{f}_d(\mathbf{r}_{i,k-1}) + \mathbf{f}_p(\mathbf{r}_{i,k-1})] \quad (38)$$

with

$$\Delta_k = (t_k - t_{k-1})/\eta, \quad (39)$$

where η is a proportionality factor and t_k is the time at instant k . The time evolution of Eqs. (38)-(39) has the physical basis of an asymptotic viscous vortex movement with a viscosity per unit length η , for which $\eta\dot{\mathbf{r}} = \mathbf{f}_e + \mathbf{f}_d + \mathbf{f}_p$ [10, 3]. In the numerical method, we implemented a self-adaptative procedure for choosing the optimum Δ_k at each time instant for a quick convergence to the stationary situation.

The elastic and driving line forces, \mathbf{f}_e and \mathbf{f}_d are calculated using Eqs. (4) and (6), respectively, and \mathbf{f}_p is evaluated taking into account that it opposes to the action of the driving force and has a maximum magnitude $f_{p,m}$. Then, the effect of \mathbf{f}_p when the driving line force is smaller than $f_{p,m}$ is to avoid any vortex deformation for $|\mathbf{f}_d| \leq f_{p,m}$ and for higher \mathbf{f}_d , \mathbf{f}_p reduces the effect of the driving force by $f_{p,m}$.

4.2 Critical current calculation

For a vortex breaking phenomenon, the critical current J_c is the maximum J for which there exists a stable vortex line configuration. A current above J_c creates a driving force per unit length that cannot be balanced by neither the elastic nor the pinning ones and the vortex moves or deforms indefinitely.

According to this, the critical current is calculated as follows. We take a J interval with one boundary below J_c , J_{\min} , and the other one above, J_{\max} . Then, we choose a certain current between them, J' , and calculate the vortex distribution. If the vortex line for $J = J'$ converges to a stable solution, we change J_{\min} into J' and J_{\max} into J' , otherwise. Thus, the interval containing J_c is narrowed. In order to ensure a solution of the procedure, we choose a very wide initial interval, with $J_{\min} = 10^3$ A/m² and $J_{\max} = 10^{15}$ A/m². We found that the number of vortex line calculations is minimized by taking J' as the middle point in logarithmic scale, $J' = \sqrt{J_{\min}J_{\max}}$. The number of vortex line evaluations for obtaining a 1% wide interval is around 12.

Numerical calculations showed that the J_c result do not significantly change with the number of vortex elements n . The computing time for $n = 20$ in an standard table computer is of few seconds (around 15s), allowing a systematic study of the J_c dependence with the applied magnetic field orientation.

4.3 Results

4.3.1 Vortex bending

Although the numerical method described above is valid for any relative orientation between \mathbf{J} and \mathbf{B} , here we restrict our study for \mathbf{B} in the xy plane of Fig. 1, that is, $\theta = \pi/2$. This corresponds to the experimental situation of a thin film YBCO bicrystal with the applied field parallel to the surface and, consequently, the ab planes.

In Fig. 6 we present the vortex bending at $J = J_c$ for several φ orientations. In the plots, the x' axis is in the direction of the applied magnetic field and the y' axis is perpendicular to both x' and z , Fig. 1.

The situation in Fig. 6(a) is for \mathbf{J} almost perpendicular to the field, with $\varphi = 0.02\pi(3.6^\circ)$. It can be seen that the vortex line bends almost exclusively in the z direction, following a half circle with a diameter equal to the vortex length in the LPR, D , as predicted analytically in Sec. 3.1. When \mathbf{J} makes an intermediate angle with \mathbf{B} , as in Fig. 6(b), the vortex also bends antisymmetrically in the y' direction and the maximum deformation in the z axis is smaller than D . Another interesting situation is when \mathbf{J} is almost parallel to \mathbf{B} , as shown in Fig. 6(c) for which $\varphi = 0.49\pi(88.2^\circ)$. For this limit, the vortex approaches to an helix with twist pitch $-D$. This result justifies the helical vortex assumption for the analytical deduction in Sec. 3.2.

4.3.2 Critical current density

In the following we study first J_c with null pinning in the LPR and then we consider the effect of a finite $f_{p,m}$. Below, we refer to J_c for $f_{p,m} = 0$ as the breaking current density, J_{break} .

In order to study the general breaking behaviour in a GB, in Fig. 7 (solid line plus symbols) we present J_{break} normalized to the breaking current density at the force-free situation $J_{\text{break,ff}} = 2\pi\epsilon_l/(d\Phi_0)$ [Eq. (37)] as a function of the angle φ (see sketch in Fig. 1). Such representation is universal for any d and ϵ_l . This can be seen as follows. J_{break} is the maximum J at which the elastic line force compensates the driving one. Since the elastic line force is proportional to ϵ_l , the same must be for J_{break} . Besides, the whole vortex line configuration at $J = J_c$ scales with the LPR thickness d . Since f_e is proportional to the vortex line curvature and twisting, f_e and, thus, J_{break} must be inversely proportional to d . Consequently, J_{break} is proportional to ϵ_l/d and to $J_{\text{break,ff}} = 2\pi\epsilon_l/(d\Phi_0)$.

The maximum J_{break} (Fig. 7) is for $\varphi = \pi/2$, corresponding to \mathbf{J} parallel to \mathbf{B} . As can be seen in the figure, the J_{break} value at the maximum is $J_{\text{break,ff}}$, in accordance to the analytical deduction in Sec. 3.1.

The numerically calculated $J_{\text{break}}/J_{\text{break,ff}}$ of Fig. 7 can be well fitted by the expression

$$J_{\text{break}}/J_{c,ff} = \frac{1}{\pi} \tan |0.78\varphi| + \frac{0.22}{\pi} \sin |\varphi|, \quad (40)$$

corresponding to the dash line in Fig. 7. The difference between the analytical fit and the numerical data decreases with decreasing φ , being of a 5% for $\varphi = \pi/2$ and less than 1.3% for $|\varphi| \leq 0.4\pi(72^\circ)$.

We next study the effect of including a pinning force in the LPR. In Fig. 7 we plot $J_c/J_{c,ff}$ for a nonzero $f_{p,m}$ [$f_{p,m}/(\Phi_0 J_{c,ff}) = 0.02, 0.1$], showing a roughly uniform increase of J_c by $f_{p,m}/\Phi_0$ in most of the $J_c(\varphi)$ curve except close to $\varphi = \pi/2$, where J_c diverges. This behaviour can be explained as follows. If $f_{p,m}$ is large enough to counteract the driving force, the vortex stays as a straight line. Otherwise, the vortex bends and the elastic force adds to the pinning one. However, the deformation of the vortex does not always lead to a compensation of the driving force. Indeed, for \mathbf{J} almost parallel to \mathbf{B} and high enough

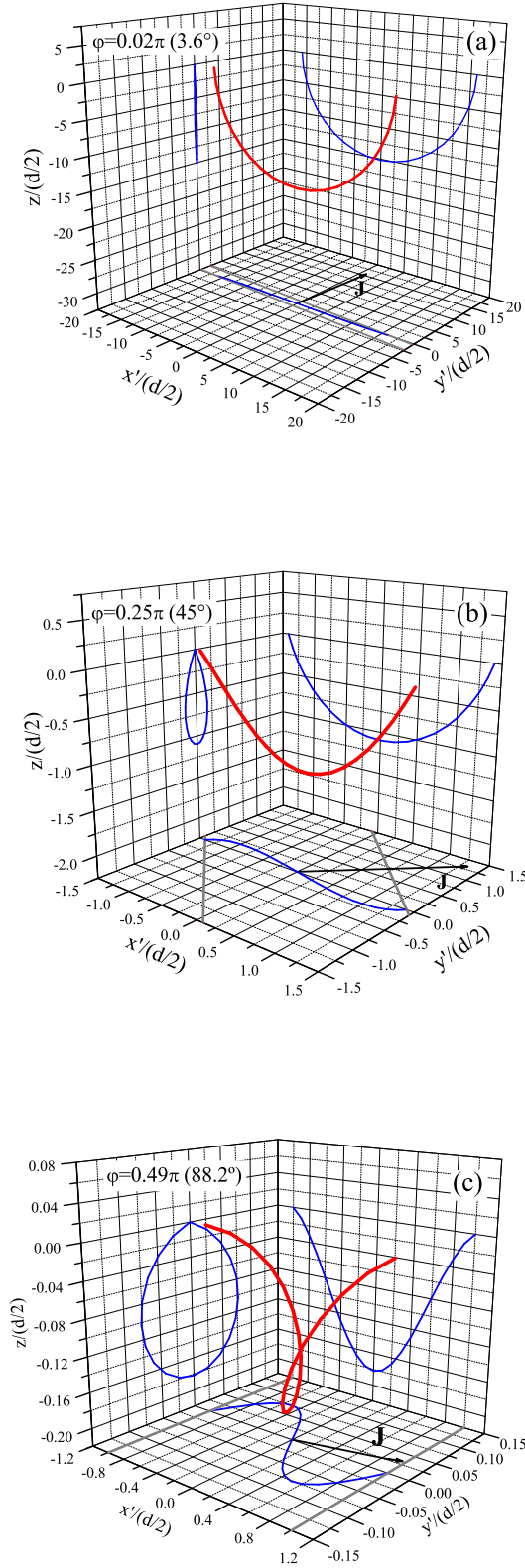


Figure 6: Vortex deformation for the situation of Fig. 1 at $J = J_c$ for $\theta = \pi/2$ and several φ angles (red thick lines), where all dimensions have been normalized to the GB half width $d/2$. Blue thin lines are the projections in the $x'z$, $x'y'$ and $y'z$ planes, the black arrow shows the current direction and the grey lines show the LPR-HPR boundaries in the $x'y'$ plane. In (c), note the different scales of the axis.

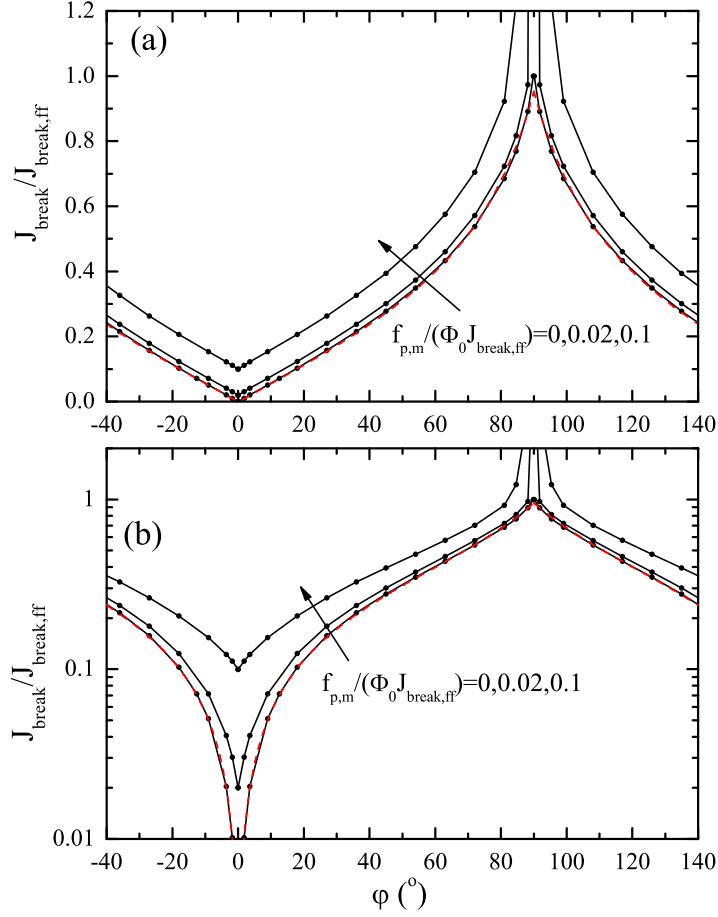


Figure 7: Calculated critical current density, J_c , for $\theta = \pi/2$ as a function of φ for the situation of Fig. 1. The curves are universal, for any d and ϵ_l when, J_c is normalized to the critical current density in the force-free configuration $J_{\text{break,ff}}$, expressed by Eq. (37). Lines plus symbols are for numerically calculated data for $f_{p,m}/(\Phi_0 J_{\text{break,ff}}) = 0, 0.02, 0.1$ from bottom to top and the dash red line is for the analytical fit of Eq. (40).

J , the vortex deforms helically and experiences a higher driving force than when it was straight. Then, for this situation the critical current density is determined by depinning, so that $J_c = f_{p,m}/(\Phi_0 |\cos \varphi|)$ and J_c diverges for $\varphi = \pi/2$. For the orientations that flux breaking exists, the increase in the numerically calculated J_c due to pinning in the LPR fits well to $f_{p,m}/(\Phi_0 \sqrt{|\cos \varphi|})$. Thus, taking into account the above features and Eq. (40) for J_{break} , J_c can be well described by

$$J_c = \max(J_{c,1}, J_{c,2}) \quad (41)$$

with

$$J_{c,1} = \frac{f_{p,m}}{\Phi_0 |\cos \varphi|} \quad (42)$$

$$J_{c,2} = \frac{2\epsilon_l}{d\Phi_0} (\tan |0.78\varphi| + 0.22 \sin |\varphi|) + \frac{f_{p,m}}{\Phi_0 \sqrt{|\cos \varphi|}}. \quad (43)$$

Comparing Eq. (43) and equation (22) for low magnetic field orientations φ , it can be seen that for the low- φ limit they are coincident and they differ less than 2% and 8% for $\varphi < 15^\circ$ and $\varphi < 30^\circ$, respectively.

If we take into account that the pinning line force in the HPR has a finite value, the critical current density cannot be larger than that limited by depinning in the HPR (Sec. 3.1.2). Thus, J_c will have the lower value between those given by Eqs. (41)-(43) and $f_{p,m}^*/(\Phi_0 |\cos \varphi|)$.

5 Application to experimental situations

In this section we apply the theoretical model developed in Secs. 3 and 4 to the experimental situations of LAGB and vicinal films in YBCO. The deduced $J_c(\theta, \varphi)$ is fitted to the measured data in order to obtain the vortex line tension in these systems.

5.1 Low-angle grain boundaries

The study of low-angle grain boundaries is of great practical importance because they are present in YBCO coated conductors [25], which are the most promising high-temperature superconducting materials for applications in electrical devices [26]. Indeed, grain boundaries are limiting the critical current density in coated conductors.

The geometry described in this article can be directly applied in order to model low-angle grain boundaries in YBCO bicrystals. In these grain boundaries there are Abrikosov-Josephson vortices (AJV) [20], which magnetic extent and normal core is of larger size than the usual Abrikosov vortices and, thus, the AJV in the grain boundary presents lower pinning than the AV in the grains [20, 27]. Assuming a sharp transition between the grain and the grain boundary, this situation corresponds to the HPR/LPR/HPR layered structure in Fig. 1. Actually, for the Abrikosov-Josephson vortices in LAGB introduced in Ref. [20] it is assumed that the vortices in the crystals are conventional AV and parallel to the boundary plane. The AJV theory in Ref. [20] is, then, directly applicable to high-temperature superconductors for magnetic inductions and LAGB parallel to the c crystallographic axis. For \mathbf{B} in the ab plane, the vortices in the crystals are not AV but Josephson string vortices (SV), which complicates the description near a LAGB. However, it is expected that SV in a LAGB will present a larger phase core and magnetic extent in the LAGB direction. This significantly changes the SV properties, as follows.

The supercurrents around SVs flow in two characteristic penetration depths, λ_{ab} in the c axis direction and $\lambda_c = \Gamma \lambda_{ab}$ in the ab plane [3, 4]. In SVs, the phase core have a size of $d_{\parallel 1}$ in the c axis and $\Gamma d_{\parallel 1}$ in the ab planes, where $d_{\parallel 1}$ is the separation between ab layers. SV are,

then, highly anisotropic. A LAGB perpendicular to the SV and parallel to the c axis will enlarge both the penetration depth and the phase core in the c direction, reducing the SV anisotropy. Furthermore, SVs present a strong intrinsic pinning towards driving forces in the c direction owing to the reduced order parameter between ab planes. Therefore, increasing the SV phase core in the c direction due to a LAGB will significantly reduce the intrinsic pinning. If the SVs are making a certain angle φ with the LAGB, the situation is even more complex but for not very large φ it is expected a significant intrinsic pinning reduction with a weak φ dependence.

5.1.1 Comparison with experiments

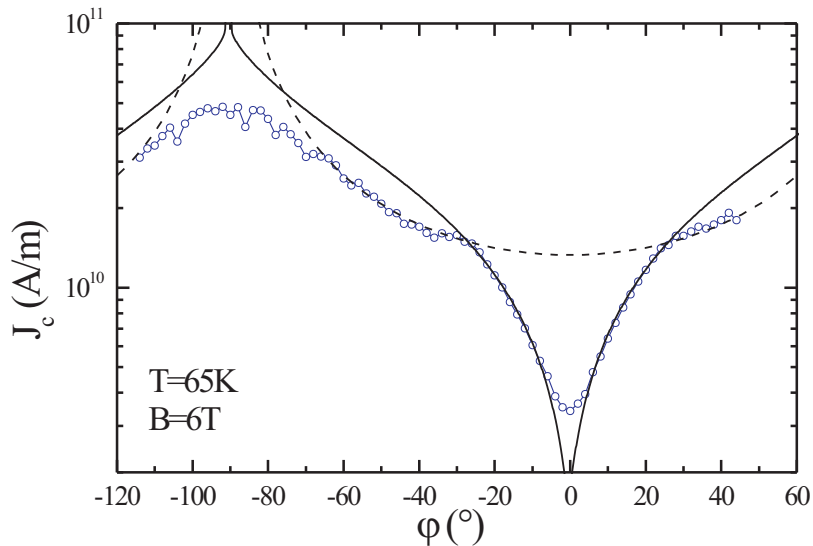


Figure 8: Measured J_c for a grain boundary in an YBCO bicrystal with a 4.9° misorientation angle [21] (hollow blue circles) together with the theoretical fit for breaking in the LAGB (solid line), calculated from Eqs. (41)-(43), and for depinning in the crystals (dash line), from $J_c = f_{p,m}^*/(|\Phi_0| \cos \varphi)$. The fit parameters are $\epsilon_l = 2.89 \times 10^{-13}\text{N}$, $f_{p,m} = 3.1 \times 10^{-6}\text{N/m}$ and $f_{p,m}^* = 2.8 \times 10^{-5}\text{N/m}$.

The J_c numerical results from Fig. 7 (Sec. 4.3), or the equivalent formulae (41)-(43), can be used for fitting experimental data for grain boundaries and extract the vortex line tension ϵ_l . In Fig. 8 we fit the experimental $J_c(\varphi)$ dependence for a low angle GB in an YBCO bicrystal [21] with our numerical curve, obtaining $\epsilon_l = F_{\text{break}}/2 = 2.89 \times 10^{-13}\text{N}$, $f_{p,m} = 3.1 \times 10^{-6}\text{N/m}$ and $f_{p,m}^* = 2.8 \times 10^{-5}\text{N/m}$ for a temperature $T = 65\text{K}$ and an applied magnetic field $B = 6\text{T}$. From the fitting parameters and Eq. (29) a maximum flux breaking angle of $\varphi_d = 25.5^\circ$ is obtained, corresponding to the measured value in Fig. 8. Moreover, the experimental results from [21] are field independent in the measured range (1 to 5T). This can be explained by the low vortex separation compared to λ_{ab} , which causes that the line tension is mainly the vortex core energy, as discussed in Sec. 2.2.

It is interesting to compare the fitted value of ϵ_l with the expected one for an anisotropic vortex. Using a λ_{ab} temperature dependence of

$$\lambda_{ab} = \lambda_{ab,0}(1 - T/T_c)^{-1/2} \quad (44)$$

with $\lambda_{ab,0} = 1.50 \times 10^{-7}\text{m}$ and $T_c = 91\text{K}$, Eq. (10) yields $\epsilon_l \approx 1.72 \times 10^{-11}\text{N}$, which is two orders of magnitude larger than the value obtained from the experimental data. However, a

better agreement is found when assuming an isotropic vortex with a magnetic size $\lambda_c = \Gamma\lambda_{ab}$, obtaining $\epsilon_l \approx \epsilon_{l,0} = 1.38 \times 10^{-13}\text{N}$. This is consistent with a significant vortex anisotropy loss due to a vortex size increase in the c direction, caused by the LAGB (Sec. 5.1). However, the origin of this discrepancy might be the oversimplified analysis in the deduction of Eqs. (10)-(11) for the line tension. A more accurate prediction would require a further complicated discussion on the vortex lattice elasticity [13, 14, 4].

5.2 YBCO films with miscut substrate

Another system which spontaneously presents flux breaking is an YBCO film on a miscut substrate [28, 22], commonly named a vicinal film. It is well known that for applied fields with an orientation angle with the ab planes below around 11° , the vortex line in YBCO have a stair-like shape, composed by pancake vortices (PV) in the ab planes and string vortices (SV) between these planes [3]. While pancake vortices are strongly pinned, this is not the case for the string ones. Although a large pinning force is required to depin SVs from the ab plane direction, they are almost free of pinning for forces parallel to the ab planes. The result is that the SV is a weakly pinned vortex segment confined between two ab planes with its ends strongly pinned by pancake vortices. Therefore, under the presence of a transport current with a component in the c direction, the SVs will bend in the ab plane and, eventually, break for a transport current density above a certain threshold⁴, J_c .

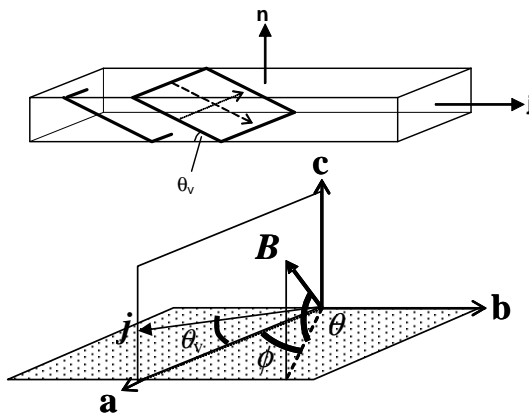


Figure 9: Sketch of a vicinal film and description of the angular coordinates θ and φ .

5.2.1 Breaking description for vicinal films

Due to intrinsic pinning, the driving force will deform the SV mainly in the ab plane following a circular arch, as shown in Fig. 10(a,b). If we restrict our analysis to the vortex deformation in the ab planes only, a SV would expand until it finds another string vortex in the same plane. However, flux crossing will occur much sooner if we consider the interaction between SV in different planes. For $J = J_c$, Fig. 10(b), the SVs between different planes are antiparallel at the junction with the common pancake vortex, where they experience a strong attractive interaction. This attraction compensates, at least partially, the bowing effect of the driving force and antiparallel straight SV segments appear 10(c). When the length of these segments is large enough, the SV attraction will overcome the intrinsic pinning and they will cross-join, creating a pair of unpinned pancake-antipancake vortices 10(d). The new pancake follows the

⁴If the YBCO film is grown on a normal substrate, the transport current flows parallel to the ab planes and there is no breaking phenomenon. For this reason, it is required a miscut angle in the substrate in order to obtain a certain component in the c direction and observe vortex breaking.

whole vortex drift, while the antivortex approaches to the original pinned pancake, annihilating to each other. Finally, we obtain a depinned vortex with undeformed SV segments, Fig. 10(e), for a driving force much lower than that one required for pancake depinning.

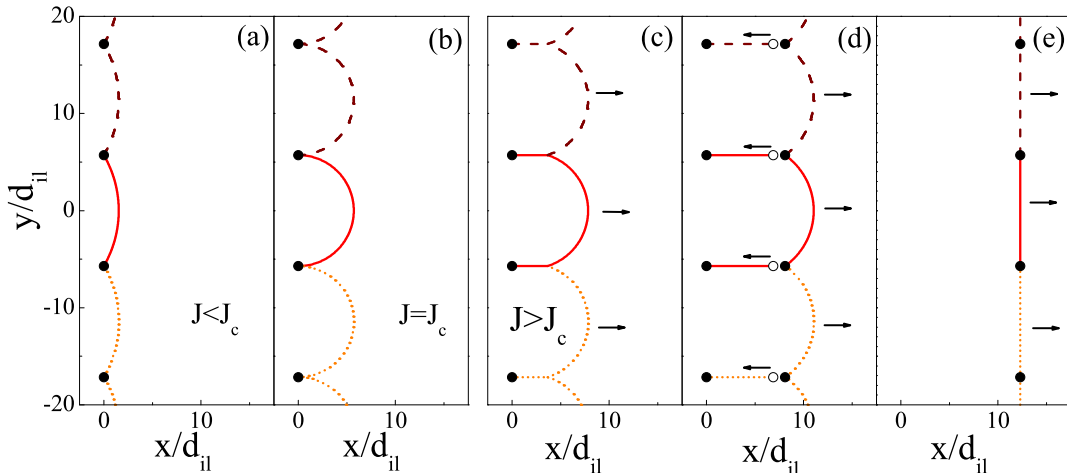


Figure 10: Static vortex deformation (a,b) and proposed breaking and cross-joining process (c,d,e) for a string vortex (SV) in a vicinal film with a field orientation $\theta = 10^\circ$, Fig. 9. The graph is the projection in the ab plane of a kinked vortex, where lines are SV between a - b planes and circles are pancake vortices. The solid (red) lines are for SVs in the graph plane, dash (maroon) ones are for SV at lower planes and dot (orange) lines are SV in higher planes. Solid and hollow dots are pancake vortices and antivortices, respectively.

This vortex breaking and cross-joining process is set up when the driving line force is larger than the sum of the maximum elastic and pinning line forces. Using the angular coordinates of Fig. 9, the driving line force in a SV is $\mathbf{f}_d = \Phi_0 J \sin \theta_v \mathbf{b}$, where θ_v is the vicinal angle and \mathbf{b} is the unit vector in the b axis. From Eq. (18), we obtain that the maximum elastic line force is $\mathbf{f}_e = -(2\epsilon_l/d_{||})|\tan \theta|\mathbf{b}$, where $d_{||}$ is the a - b interlayer distance. Considering this and a certain pinning force, we obtain the following critical current density

$$J_c = \frac{2\epsilon_l}{d\Phi_0 \sin \theta_v} |\tan \theta| + \frac{f_{p,m}}{\Phi_0 \sin \theta_v}, \quad (45)$$

consistent with the expression in Refs. [22, 28] with a total SV breaking force of $2\epsilon_l$.

5.2.2 Comparison with experiments

The model introduced above can be applied in order to obtain ϵ_l for a SV, as follows. In Fig. 11 we present the measured $J_c(\theta)$ for an YBCO vicinal film with 4° miscut substrate [28]. In this figure we include the fitting curve for the breaking limited $J_c(\theta)$ of Eq. (45) (solid line) together with the fitted $J_c(\theta)$ for a kinked vortex depinning (dash line), calculated using [28]

$$J_c = \frac{f_{p,\text{str}} \cos \theta + f_{p,\text{pc}} \sin |\theta|}{\Phi_0 \sin |\theta - \theta_v|}, \quad (46)$$

where $f_{p,\text{str}}$ and $f_{p,\text{pc}}$ are the pinning force per unit length for the string and pancake vortices, respectively, and θ_v is the substrate miscut angle. The measured data of Fig. 11 is optimally

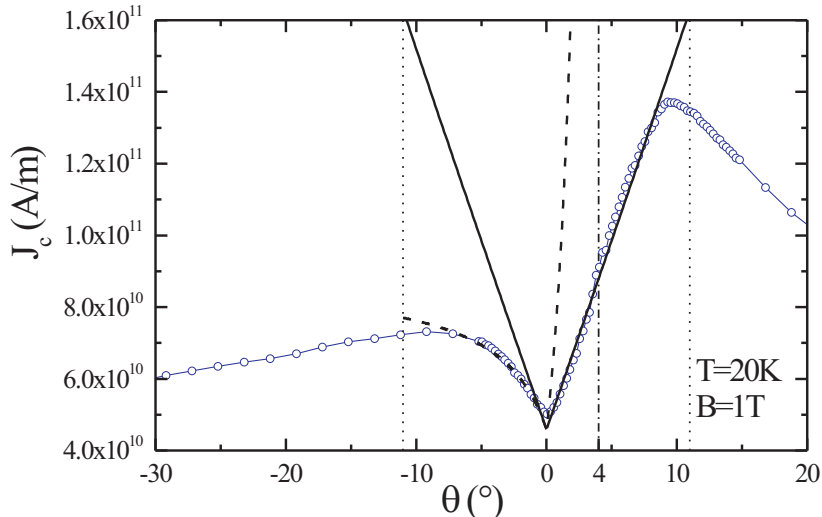


Figure 11: Measured $J_c(\theta)$ for an YBCO vicinal film with 4° miscut substrate [28] (line with circles) together with the fitting curve for the breaking limited J_c of Eq. (45) (solid line) and the fit for a kinked vortex depinning (dash line), calculated using Eq. (46). The fitting parameters are $\epsilon_l = 1.69 \times 10^{-14}\text{N}$, $f_{p,\text{str}} = 6.62 \times 10^{-6}\text{N/m}$ and $f_{p,\text{pc}} = 1.82 \times 10^{-4}\text{N/m}$.

fitted by Eqs. (45) and (46) with $\epsilon_l = 1.69 \times 10^{-14}\text{N}$, $f_{p,\text{str}} = 6.62 \times 10^{-6}\text{N/m}$ and $f_{p,\text{pc}} = 1.82 \times 10^{-4}\text{N/m}$. The two vertical dot lines in Fig. 11 delimit the expected angular region where kinked vortices can exist ($\theta \approx 11^\circ$)[3], while the dash-dot line indicates the θ value at which the kinked vortex presents null total driving force, $\theta = \theta_v$, so that the depinning-limited J_c diverges. Thus, it is clear that for this situation the limiting mechanism of J_c must be flux breaking. Besides, both Eqs. (45) and (46) for string vortex breaking and kinked vortex depinning, respectively, fit to the experimental data for the range $|\theta| < 9^\circ$; a slightly smaller value than the originally expected $|\theta| \approx 11^\circ$.

The expected SV line tension in the parallel direction from Eqs. (11) and (44) is $\epsilon_l \approx 1.9 \times 10^{-12}\text{N}$, which is around two orders of magnitude larger than the obtained one from Fig. 11. This discrepancy, also found in Sec. 5.1, evidences that the use of the simplified Eqs. (9)-(11) is probably too naïve and a more detailed study of the line tension in terms of the flux line lattice elasticity is required for a fine prediction.

6 Conclusions

One way of studying the superconducting vortex lattice properties is by vortex breaking experiments in nonuniform pinning force distributions.

In this article, the vortex bending and breaking in a high-pinning/low-pinning/high-pinning layered structure has been studied from a microscopical point of view in order to extract vortex internal properties from breaking experiments. Our study has been based on an elastic model assuming a constant vortex line tension, ϵ_l . For the general 3D bending, this model is applicable for isotropic superconductors in the single-vortex approximation. The latter approximation can be done for a magnetic penetration depth λ much larger than the vortex separation because for this case the vortex line energy is mainly the core energy. As a consequence, the line tension is independent on both the vortex deformation amplitude and the deformation length. Within the assumption of constant line tension, the model is

applicable to any nonuniform pinning force or current density distribution.

Summarizing, the main results from the elastic model are the following.

When the pinning force in the high-pinning regions (HPRs) is much higher than that in the low-pinning ones (LPR), the vortex only bends in the LPR. For low magnetic field orientation angles with the HPR-LPR boundary (φ), the vortex takes the shape of a circular arch with a minimum curvature radius of half the LPR thickness. The latter situation corresponds to the maximum elastic force. For a transport current J higher than the value which this happens (J_c), the elastic force cannot balance the driving one and the vortex moves until it finds its neighbour. After this, we have proposed that the adjacent vortices cross-join and recombine with an steady average vortex movement in the LPR. For higher \mathbf{B} orientation angles $|\varphi|$, there is a similar behaviour, with the difference that the vortex deforms in two orthogonal directions. When φ is close to $\pi/2$, corresponding to the force-free configuration, the vortex experiences a helical deformation with a small radius. For the case that φ is exactly $\pi/2$, the vortex presents a helical instability for J above a certain threshold and keeps as a straight line for J below.

The more realistic case of finite pinning force in the HPR presents vortex bending in both in the LPR and the HPRs. For this case, if the maximum elastic line force in the LPR is larger than the pinning line force difference, the vortices present depinning in the HPR above a certain orientation angle φ_d . When the orientation angle is slightly lower than φ_d , the vortex bends in the HPR over a thickness larger than that of the LPR.

The model calculations have been used for obtaining the vortex line tension in two experimental situations: a low-angle grain boundary (LAGB) in an YBCO bicrystal and an YBCO film on a miscut substrate. In these systems the vortices involved are vortices of Abrikosov-Josephson nature and string vortices.

For LAGB with a low angle φ between the magnetic field and the grain boundary plane, the vortex mainly bends in one single direction and the constant line tension assumption is reasonable. The line tension obtained by fitting the modelled curve with the measured data is much smaller than the expected one for an anisotropic vortex from Eq. (10), although ϵ_l is of the same order of magnitude as an isotropic vortex with penetration depth λ_c . This result is consistent with an anisotropy loss due to a vortex enlargement in the c crystallographic axis. However, it must be kept in mind that the applicability of the simplified equations (10)-(11) is not evident for the studied LAGB situation.

The results for YBCO films with a miscut angle show again that the line tension is two orders of magnitude lower than expected. This reinforces the hypothesis that Eqs. (10)-(11) are not applicable for SVs at the studied temperature and magnetic field conditions, for which the vortices are strongly overlapped. Thus, a more complex analysis in terms of the flux line lattice elasticity should be done for performed for a proper prediction of the line tension.

In conclusion, modelling based on the vortex elastic properties provides a good explanation for the flux breaking phenomena. In this article, the elastic theory has been successfully applied for obtaining the line tension of “exotic” vortices, such as string vortices between ab planes and in low-angle grain boundaries.

References

- [1] A. A. Abrikosov, Zh. Eksp. Teor. Fiz. **32** 1442 (1957) [English translation: A. A. Abrikosov, Sov. Phys. – JETP **5**, 1174 (1957)].
- [2] A. M. Campbell and J. E. Evetts, Adv. Phys. **21**, 199 (1972) [Reprint: A. M. Campbell and J. E. Evetts, Adv. Phys. **50**, 1249 (2001)].

- [3] G. Blatter, M.V. Feigel'man, V.B. Geshkenbein, A.I. Larkin, V.M. Vinokur, *Rev. Mod. Phys.* **66**, 1125 (1994).
- [4] E. H. Brandt, *Rep. Prog. Phys.* **58**, 1465 (1995).
- [5] J. R. Clem, *J. Low Temp. Phys.* **18**, 427 (1975).
- [6] C. R. Hu, *Phys. Rev. B* **6**, 1756 (1972).
- [7] E. H. Brandt, J. R. Clem and D. G. Walmsley, *J. Low Temp. Phys.* **37**, 43 (1979).
- [8] J. R. Clem, *J. Low Temp. Phys.* **38**, 353 (1980).
- [9] P. Wagenleithner, *J. Low Temp. Phys.* **48**, 25 (1982).
- [10] M. Bou-Diab, M.J.W. Dodgson, and G. Blatter, *Phys. Rev. Lett.* **86**, 5132 (2001).
- [11] E. H. Brandt, *J. Low Temp. Phys.* **26**, 709 (1977).
- [12] E. H. Brandt, *J. Low Temp. Phys.* **26**, 735 (1977).
- [13] A. Sudbø and E. H. Brandt, *Phys. Rev. Lett.* **66**, 1781 (1991).
- [14] A. Sudbø and E. H. Brandt, *Phys. Rev. B* **43**, 10482 (1991).
- [15] J. W. Ekin and J. R. Clem, *Phys. Rev. B* **12**, 1753 (1975).
- [16] R. Busch, G. Ries, H. Werthner, G. Kreiselmeyer, and G. Saemann-Ischenko, *Phys. Rev. Lett.* **69**, 522 (1992).
- [17] D. López, G. Nieva, F. de la Cruz, H. J. Jensen, and D. O'Kane, *Phys. Rev. B* **50**, 9684 (1994).
- [18] S. A. Grigera, T. S. Grigera, E. F. Righi, G. Nieva, and F. de la Cruz, *Physica C* **371**, 237 (2002).
- [19] M. G. Blamire and J. E. Evetts, *Phys. Rev. B* **33**, 5131-5133 (1986).
- [20] A. Gurevich, M. S. Rzchowski, G. Daniels, S. Patnaik, B. M. Hinaus, F. Carillo, F. Tafuri, and D. C. Larbalestier, *Phys. Rev. Lett* **88**, 097001 (2002).
- [21] J. H. Durrell, M. J. Hogg, F. Kahlmann, Z. H. Barber, M.G. Blamire, and J. E. Evetts, *Phys. Rev. Lett.* **90**, 247006 (2003).
- [22] J. H. Durrell, E. Pardo, J. E. Evetts and M. G. Blamire, *J. Phys.: Conf. Ser.* **43**, 627 (2006).
- [23] D. G. Walmsley, *J. Phys. F: Metal Phys.* **2**, 510 (1972).
- [24] J. R. Clem, *Phys. Rev. Lett.* **38**, 1425 (1977).
- [25] J. E. Evetts, *Supercond. Sci. Technol.* **17**, S315 (2004).
- [26] J. R. Hull, *Rep. Prog. Phys.* **66**, 1865 (2003).
- [27] A. Díaz, L. Mechin, P. Berghuis, and J. E. Evetts, *Phys. Rev. B* **80**, 3855 (1998).
- [28] J. H. Durrell, G. Burnell, V. N. Tsaneva, Z. H. Barber, M. G. Blamire, and J. E. Evetts, *Phys. Rev. B* **70**, 214508 (2004).